Forest response to rising CO_2 drives zonally asymmetric rainfall change over tropical land

Authors

Gabriel J. Kooperman[1,2]*, Yang Chen[1], Forrest M. Hoffman[3,4], Charles D. Koven[5], Keith Lindsay[6], Michael S. Pritchard[1], Abigail L. S. Swann[7], and James T. Randerson[1]

Author affiliations

[1] Department of Earth System Science, University of California, Irvine

[2] Department of Geography, University of Georgia

[3] Computational Earth Sciences Group and Climate Change Science Institute, Oak Ridge National Laboratory

[4] Department of Civil and Environmental Engineering, University of Tennessee

[5] Earth Sciences Division, Lawrence Berkeley National Laboratory

[6] Climate and Global Dynamics Division, National Center for Atmospheric Research

[7] Department of Atmospheric Sciences, University of Washington

Corresponding author

Gabriel J. Kooperman

University of Georgia

Department of Geography

kooperman@uga.edu

Abstract

Understanding how anthropogenic CO_2 emissions will influence future precipitation is critical for sustainably managing ecosystems, particularly for drought-sensitive tropical forests. Although tropical precipitation change remains uncertain, nearly all models from the Coupled Model Intercomparison Project Phase 5 predict a strengthening zonal precipitation asymmetry by 2100, with relative increases over Asian and African tropical forests and decreases over South American forests. Here we show the plant-physiological response to increasing CO_2 is a primary mechanism responsible for this pattern. Applying a simulation design in the Community Earth System Model in which CO_2 increases are isolated over individual continents, we demonstrate that different circulation, moisture, and stability changes arise over each continent due to declines in stomatal conductance and transpiration. The sum of local atmospheric responses over individual continents explains the pan-tropical precipitation asymmetry. Our analysis suggests that South American forests may be more vulnerable to rising CO_2 than Asian or African forests.

The response of the hydrological cycle to increases in the concentration of atmospheric CO_2 has consequences for global food security and the sustainability of terrestrial ecosystems. In particular, changes in the patterns of precipitation and evapotranspiration may influence the frequency of droughts[1], forest mortality[2], and freshwater availability[3]. These impacts are especially important in the tropics, where many developing countries are hotspots for climate change vulnerability[4] and where forests are critical for global carbon cycling[5] and biodiversity[6].

Unfortunately, projections of future precipitation and evapotranspiration from Earth system models participating in the Coupled Model Intercomparison Project Phase 5 (CMIP5[7]) are most uncertain over tropical land[8,9]. Although multi-model mean changes in annual mean precipitation

during the 21st century driven by the RCP8.5 scenario (Fig. 1) can be larger than 1 mm day^{-1}, many models predict opposing changes over tropical forests[8], especially American and African forests where six and ten of 38 models have responses opposite to the multi-model mean, respectively (Fig. 1, Fig. S1, and Tables S1 and S2).

Robust tropical precipitation change

Despite this uncertainty, we have identified a robust pattern of change captured in nearly all high emissions simulations – a growing zonal asymmetry that amplifies precipitation differences between tropical forests in South America and those in Asia and Africa (Fig. 1a-c). Focusing on forests in Amazon and Indonesian regions (with the latter including Indonesia, Malaysia, and Papua New Guinea), this pattern can be quantified using a tropical precipitation asymmetry index (I_{TPA}): $I_{TPA} = P_{Indonesia} - P_{Amazon}$, where P is annual mean precipitation over forest regions (i.e., green areas within purple boxes in Fig. 1f). Present (1986-2005) and future (2081-2100) precipitation estimates (Fig. 1g) show that, in 36 out of 38 models that were run for the RCP8.5 scenario, I_{TPA} shifts to more positive values, with a multi-model mean of 1.1 [-0.3, 2.5] mm day^{-1} (brackets denote model range; Tables S1 and S2).

More broadly across all tropical forests from 23˚S to 23˚N, including Africa (i.e. $I_{TPA2} = (P_{Asia} + P_{Africa})/2 - P_{America}$, averaged over forest regions within black boxes in Fig. 1f), all RCP8.5 simulations have positive but smaller index increases in asymmetry, with a multi-model mean of 0.7 [0.1, 1.3] mm day^{-1} (Fig. S1 and Table S2). Similarly, in idealized simulations in which CO_2 increases at a rate of 1% $year^{-1}$ from 285 to 1140 ppm (hereafter referred to as Full simulations), all but one model captures a consistent positive trend in I_{TPA}, with a multi-model mean of 1.5 [-0.6, 2.4] mm day^{-1} (Fig. 1h). Eight Earth system models were run following the

Full simulation protocol, with the primary goal of understanding carbon cycle feedbacks[11]. The spatial pattern of precipitation change from the Full simulations (Fig. 1c) has a high degree consistency with the spatial pattern from the same set of models that were run for the RCP8.5 scenario (Fig. 1b), thus highlighting the importance of forcing from atmospheric CO_2 as a primary agent of tropical (and global) precipitation change.

Though CMIP5 models use convective parameterizations that are known to produce biases in the tropics, which can impact soil moisture, evapotranspiration, and runoff[8,9,12], an increase in I_{TPA} is also seen in a model that avoids parameterization by explicitly simulating deep convection using a kilometer-scale embedded cloud resolving model (i.e., superparameterization[13], squares in Figs. 1g and S1). Superparameterization improves the representation of organized convection (e.g., Madden Julian Oscillation[13]) and precipitation intensity across the tropics[14]. Consistency between superparameterized and conventional models suggests that the strengthening continental asymmetry in precipitation change is robust with respect to the representation of convection.

Mechanisms of precipitation change

Many studies have investigated mechanisms that drive changes in tropical precipitation, including: changes in the strength of Hadley[15] or Walker circulations[16], shifts in the inter-tropical convergence zone (ITCZ)[17], or wet-get-wetter responses[18]. These changes involve global or extra-tropical forcings[15,17], tropics-wide circulation anomalies[16], and local thermodynamic responses[18,19]. Most global and extra-tropical mechanisms invoke zonal mean changes in meridional energy transport to explain changes in the strength or position of the Hadley circulation. However, zonal mean changes cannot explain the asymmetric pattern described here for tropical forests across different continents. Several recent studies have attempted to extend

93 the wet-get-wetter scaling mechanism to include horizontal gradients of temperature and
94 humidity[20] or the ITCZ shift mechanism to include zonal energy fluxes[21], but neither
95 atmospheric-centric response mechanism fully captures the pattern of change.
96 Tropics specific mechanisms, including perturbations to the Walker circulation[16] or patterns
97 of sea surface temperature[19], which could influence convection and moisture transport[22], have the
98 potential to create zonally asymmetric responses. However, local changes operating in isolation
99 over individual continents could also modify regional temperature, circulation, and moisture
100 transport, enhancing or diminishing precipitation. Local changes over the Amazon may lengthen
101 the dry season due to modulation of orographic dynamics related to the Andes[23,24] or the
102 subtropical jet[25], while changes over Asia may be associated with the intensity of the Madden
103 Julian Oscillation[26] or monsoons[27]. Additionally, thermodynamic responses associated with
104 regional changes in the horizontal gradients of temperature and humidity can influence local
105 moisture convergence by as much as these dynamical effects[20].
106
107 **Plant physiological response**
108 Plant physiological responses to rising CO_2 can contribute to precipitation changes by
109 modifying moisture convergence patterns[28], but it remains to be seen whether these changes are
110 driven by local or remote mechanisms. Here we hypothesize that plant responses are a primary
111 driver of the growing precipitation asymmetry, by exciting local circulation and thermodynamic
112 changes over individual continents. We tested this hypothesis by regionally isolating the impacts
113 of higher CO_2 in a new set of experiments with the Community Earth System Model described
114 below. Atmospheric CO_2 concentration influences the radiative properties of the atmosphere, and
115 the physiological behavior of terrestrial plants, both of which can drive changes in

precipitation[3,28,29]. The direct physiological impact of increasing CO_2 is to increase the CO_2 partial pressure outside leaf stomata. Stomata control gas exchange by adjusting the aperture of their openings in response to CO_2 and other environmental variables, and thus the rate of CO_2 uptake and H_2O loss (transpiration)[30]. This mechanism connects soil moisture in the vadose zone to the atmosphere and influences the ratio of latent to sensible heating.

As CO_2 increases, stomatal conductance often declines. Without a substantial change in other environmental conditions or leaf area, this decline may reduce the amount of moisture that escapes[31,32,33,34] and modify the surface energy budget. In temperate forests, free air CO_2 enrichment experiments show that canopy-level transpiration declines or remains neutral in mature stands as the concentration of atmospheric CO_2 increases[35]. In tropical forests, carbon isotope and tree ring growth measurements provide indirect evidence that transpiration has declined over the last 150 years in response to rising CO_2 [36]. Increases in observed tropical runoff are also consistent with an ecohydrological response to increasing CO_2[37], although changing land use can have first order impacts in many basins[38].

Physiological versus radiative impacts of rising CO_2

To test the hypothesis that the contribution of reduced stomatal conductance to a growing zonal precipitation asymmetry pattern is robust across different climate models, we analyzed carbon cycle simulations from CMIP5. We assessed the relative contribution of radiative and physiological effects on precipitation changes in three sets of simulations that were originally designed to quantify the magnitude of carbon-climate feedbacks[11] (Table S4). As described above, eight independent Earth system models contributed simulations following this protocol (Table S3). In these simulations, atmospheric CO_2 increases from 285 to 1140 ppm

(quadrupling) at a rate of 1% year^{-1}. In one set of simulations the radiative and physiological effects of CO_2 are simultaneously active (Full simulations). In another set, increasing CO_2 solely influences atmospheric radiation, while terrestrial vegetation experiences a constant pre-industrial CO_2 concentration (hereafter referred to as Radiation simulations). In a third set, increasing CO_2 solely influences terrestrial vegetation, while atmospheric radiation experiences a constant pre-industrial CO_2 concentration (hereafter referred to as Physiology simulations)[3,11].

Multi-model mean differences between the first and last twenty years of these simulations show that the pattern of precipitation change in the fully coupled simulations (Fig. 1c) is driven by a combination of physiological (Fig. 1d) and radiative (Fig. 1e) processes. Radiative effects control high-latitude precipitation changes, but tropical changes, particularly over the Amazon, respond more strongly to physiological effects (-0.5 [-0.9, -0.3] vs. -0.3 [-0.8, 0.3] mm day^{-1}, Tables S1 and S3). All models show an increase in I_{TPA} and I_{TPA2} when plant physiology responds to rising CO_2 (Fig. 1i) and all but one show an increase in these indices from atmospheric radiative responses (Fig. 1j). Physiology effects yield larger I_{TPA} increases in half of the models and a slightly larger multi-model mean change (0.9 [0.4, 1.7] mm day^{-1}) than radiative effects (0.8 [0, 1.8] mm day^{-1}).

Local versus non-local physiological effects

To determine whether the influence of physiology on the tropical precipitation asymmetry is caused by global, tropics-wide, or local-to-continental scale mechanisms, we performed a series of experiments using the Community Earth System Model version 1 (CESM[39]). In CESM, physiology contributions to I_{TPA} are larger than radiative contributions (Table S3), and the historical I_{TPA} value (black triangle in Fig. 1g) falls between the multi-model mean (black circle)

and observations (black star). In our new simulations, terrestrial vegetation experiences a CO_2 increase at a rate of 1% $year^{-1}$ up to 1140 ppm, as in the global Physiology simulation, but increases are isolated to the land surface of individual continents, as delineated by the black boxes in Fig. 1f (see methods for details).

The experiments indicate that local-to-regional scale processes have a first-order control on precipitation changes over each continent, confirming our hypothesis. Changes in mean continental tropical precipitation from the global Physiology simulation are mostly captured when CO_2 increases are isolated to individual tropical continents (Fig. 2). Approximately 87% of the increase over Indonesia from the global Physiology simulation is produced in the Asia simulation (Table S1). Similarly, 59% of the reduction over the Amazon is produced in the America simulation. Changes over South America also include precipitation increases over the Andes, which are captured by the regional physiology forcing. Additionally, non-local effects associated with the forcing over Africa further contribute to drying over the Amazon (43%, Table S1), which adds almost linearly with local impacts to equal the global Physiology response. In addition to exerting non-local controls, local changes in the Africa simulation have a similar pattern but greater magnitude compared to the global Physiology simulation.

Similarities in the patterns of change captured in each region are even more compelling than regional average changes (Fig. 2b-d). The stippling in these panels indicates where the regionally forced simulations capture at least 50% of the global Physiology change. Together, the three regionally forced simulations meet these criteria for almost 90% of grid-points that have a significant precipitation change in the Physiology simulation (Fig. 2a) between 23˚S and 23˚N. Thus, while the magnitude of the local regional change is somewhat lower in the America simulation compared to global Physiology (Table S1), the pattern is well captured. Focusing on

185 the Amazon and Indonesian regions, where physiological effects are largest, the change in I_{TPA} is
186 almost a linear combination of the three regionally forced simulations, which contribute 56%,
187 28%, and 12% to the global Physiology I_{TPA} value from Asia, America, and Africa simulations,
188 respectively. The contribution from the Africa simulation to the I_{TPA} change originates from its
189 influence on winds across the tropical Atlantic Ocean, and thus Amazon rainfall.
190
191 **Local thermodynamic and circulation anomalies**
192 Although there is large seasonal and inter-annual variability in the precipitation signal over
193 Amazon and Indonesian forests, the response to rising CO_2 is consistent across most seasons
194 (except boreal summer in the Amazon and boreal winter in Indonesia) and all phases of the El
195 Niño Southern Oscillation (Fig. 3). As discussed earlier, higher CO_2 can decrease stomatal
196 conductance and transpiration in mature forest stands, which can reduce total evapotranspiration.
197 This impact is seen clearly in simulated evapotranspiration changes over tropical forests (Fig. 4a-
198 d), which decrease by more than 0.5 mm day^{-1}. While the regions defined as forest in these
199 simulations do not change, leaf area can increase from enhanced growth at higher CO_2 levels
200 (Fig. S2). However, leaf area is high to begin with in tropical forests, so that CO_2 effects on
201 stomatal conductance have a larger relative influence on canopy conductance, and
202 evapotranspiration still declines. The magnitude of evapotranspiration changes simulated in the
203 global Physiology simulation are captured locally in the regionally forced simulations, with only
204 small non-local impacts. In response to decreases in evapotranspiration, the surface energy
205 budget also reaches a new steady state by increasing sensible heat fluxes and surface temperature
206 (Fig. S3).

As expected, lower evapotranspiration reduces a local source of moisture to the atmosphere and produces near-surface reductions in specific humidity over each continent (Fig. 4e-h). However, increased convection, collocated in regions of increased precipitation, is associated with local circulation and moisture gradient anomalies that lead to modified patterns of moisture convergence, with upper-level moisture elevated over each continent. The surface and upper-level anomalies are horizontally collocated over Indonesian and Central African forests, but over tropical South America the upper-level humidity increase is displaced over the Andes, while surface and upper-level reductions occur further east over lowland forests.

Circulation anomalies over South America and Central Africa (Fig. 4) are consistent with a convectively coupled response to enhanced latent heating in the atmosphere by deep convection centered on the equator, indicating a prominent role of equatorially trapped Kelvin and Rossby waves[40]. This pattern reflects convection in uplift regions to the west (e.g., Andes) with weak subsidence to the east (e.g., lowland Amazon forests). The local dynamic changes over Asia are weaker, but produce increased low-level convergence from the surrounding waters and greater uplift over the islands (i.e., over Sumatra, Java, Borneo, and New Guinea).

While the response of American and Asian tropical forests to rising CO_2 have little impact on the circulation of other tropical continents, Central African heating exerts some non-local influence. Anomalous eastward flow due to enhanced convective heating over Africa extends far enough across the Atlantic Ocean to counter the mean wind east of South America (Fig, 4c), and contributes to reduced moisture and subsidence over the Amazon (Fig. 4g). This amplifies the present-day influence of circulations associated with the presence of Africa on South America due simply to the proximity of these continents, and the ability of equatorial circulation anomalies, unimpeded by the Coriolis force (i.e., large Rossby radius), to act over long

distances[41]. This non-local influence contributes to reducing Amazon precipitation in the global Physiology and Africa simulations (Fig. 5a; Fig. S4).

Differences between Amazon and Indonesian forests

The response of reduced rainfall over the Amazon to local decreases in stomatal conductance is opposite to that of African and Indonesian forests. The Amazon's greater dependence on local moisture recycling[42], as well as its interaction with nearby orographic circulations[24], may make it especially sensitive to CO_2 physiological effects. The reduction from local evapotranspiration limits moisture recycling and accounts for 69% of the Amazon precipitation change in the global Physiology simulation (Fig. 5a). The remaining precipitation change is associated with a reduction in moisture convergence due to non-local influences from Africa rather than locally driven changes (Fig. 5a).

Over Indonesia however, there is little non-local influence on either evapotranspiration or moisture convergence, which are driven instead by locally forced changes (Fig. 5b). As expected, lower stomatal conductance reduces local evapotranspiration, but increased moisture convergence is larger, leading to higher precipitation over the islands. The different sensitivities of the two regions may result in part from their baseline reliance on local evaporative recycling versus non-local moisture transport as sources of water for precipitation. In simulations and observations, Indonesia receives a much higher fraction of its precipitation from moisture convergence (Table S5), which is enhanced in response to CO_2 forcing.

The decrease in precipitation over the Amazon is also supported by an increase in atmospheric stability (measured by gross moist stability[43,44]) due to an enhanced zonal moist static energy (MSE) gradient (horizontal-thermodynamic component, Fig. 5c) with higher MSE

253 over the mountain slopes to the west and lower to the east of the forest, especially in the 700-900
254 mb layer (Fig. S5-S7, see methods and supplementary information for details). In the presence of
255 strong easterlies from regional low-level flow, the enhanced zonal MSE gradient in turn
256 amplifies the efficiency of column MSE export by horizontal advection, leading to overall
257 stabilization and less rainfall over the forest. As a result, more moisture is transported up the
258 slopes of the Andes, which in combination with orographic blocking of anomalous eastward flow
259 from the Pacific, leads to more precipitation over the mountains. This produces a dipole
260 precipitation pattern over the Andes and Amazon that has previously been found in simulations
261 modifying the height of the Andes[24], simulations of the last glacial maximum and observations
262 of interannual variability[45]. On the other hand, increases in precipitation over Indonesia are
263 supported by a decrease in atmospheric stability resulting from a more bottom-heavy uplift
264 profile in the Physiology and Asia simulations (vertical-dynamic component, Fig. 5d), with no
265 contribution from the horizontal components.
266
267 **Discussion**
268 Our analysis shows that a robust feature of CMIP5 future projections is a strengthening
269 precipitation asymmetry across tropical continents, with increases in Asian and African forests
270 and decreases in lowland South American forests. Further analysis of idealized CO_2 only
271 simulations provides evidence that this pattern is driven by both radiative and physiological
272 responses to rising CO_2, which reinforce each other. Over dense tropical forests, physiological
273 effects, which reduce stomatal conductance and lower transpiration, are the largest drivers of
274 precipitation changes[28]. Increasing CO_2 at the land surface reduces local evapotranspiration by
275 similar magnitudes in all tropical forest regions. Over Indonesia, this reduction is smaller than

276 increases in moisture convergence, so precipitation increases. Over the Amazon the response is
277 more complicated. The forest depends more on local evaporation as its main moisture source, so
278 reductions in evapotranspiration directly impact precipitation. Furthermore, a geographic
279 redistribution of heat and moisture near the altitude of strong regional low-level easterly flow
280 leads to an increase in gross moist stability that is associated with suppressed convection over the
281 forest and greater moisture transport to the Andes. Remote effects from African forests further
282 reduce moisture flow and precipitation over the Amazon.

283 This analysis highlights the need to improve our understanding of the physiological response
284 of tropical trees to rising CO_2. New free air carbon dioxide experiment (FACE) measurements
285 from the tropics will be essential for reducing uncertainties in the representation of stomatal
286 conductance and photosynthesis coupling mechanisms in Earth system models. Since the
287 majority of precipitation change above tropical forests is captured by the atmospheric response to
288 local physiological forcing, regional high-resolution models that resolve orography and more
289 complex ecosystem processes may be useful tools in future work to better understand the role of
290 land-surface interactions in shaping projections of precipitation change. While previous work has
291 identified the Amazon as a region of high vulnerability for future climate change, our analysis
292 demonstrates that this regional response is completely different from other tropical forests, which
293 are more likely to experience decreasing moisture stress. Radiative and physiological responses
294 to rising CO_2 may be further amplified by land-use change and deforestation, which have also
295 been shown to reduce precipitation over the Amazon[46], increasing the prevalence of drought[1] and
296 putting the region at greater risk for forest fires[25]. All tropical forests are threatened biodiversity
297 hotspots, but the Amazon has more terrestrial plant and vertebrate species than any other region[6],
298 and thus plant physiological responses to rising CO_2 present a threat to biodiversity loss on a

299 global-scale. Furthermore, the Amazon's dominant role as a terrestrial carbon sink implies that
300 its future health may have critical consequences for the growth rate of atmospheric CO_2 and
301 global climate[5].
302

303 **References**

304 1. Allen, C. D. *et al.* A global overview of drought and heat-induced tree mortality reveals
305 emerging climate change risks for forests. *For. Ecol. Manag.* **259**(4), 660-684 (2010).
306 2. Phillips, O. L. *et al.* Drought–mortality relationships for tropical forests. *New Phytologist*
307 **187**(3), 631-646 (2010).
308 3. Swann, A. L. S., Hoffman, F. M., Koven, C. D. & Randerson, J. T. Plant responses to
309 increasing CO_2 reduce estimates of climate impacts on drought severity. *Proc. Natl. Acad.*
310 *Sci. U.S.A.* **113**(36), 10019-10024 (2016).
311 4. Diffenbaugh, N. S. & Giorgi, F. Climate change hotspots in the CMIP5 global climate model
312 ensemble. *Climatic Change* **114**, 813-822 (2012).
313 5. Cox, P. et al. Amazonian forest die back under climate-carbon cycle projections for the 21st
314 century. *Theor. Appl. Climatol.* **78**(137), 137-156 (2004).
315 6. Mittermeier, R. A. *et al.* Wilderness and biodiversity conservation. *Proc. Natl. Acad. Sci.*
316 *U.S.A.* **100**(18), 10309-10313 (2003).
317 7. Taylor, K. E., Stouffer, R. J. & Meehl, G. A. An overview of CMIP5 and the experiment
318 design. *Bull. Amer. Meteor. Soc.* **93**, 485-498 (2012).
319 8. Stocker, T. F. *et al.* Eds. *Climate Change 2013: The Physical Science Basis.* Cambridge
320 Univ. Press, Cambridge, U.K. (2013).
321 9. Yin, L., Fu, R., Shevliakova, E. & Dickinson, R. E. How well can CMIP5 simulate
322 precipitation and its controlling processes over tropical South America? *Clim. Dyn.* **41**(11),
323 3127-3143 (2013).
324 10. Lintner, B. R., Langenbrunner, B., Neelin, J. D., Anderson, B. T., Niznik, M. J., Li, G., &
325 Xie, S.-P. Characterizing CMIP5 model spread in simulated rainfall in the Pacific

Intertropical Convergence and South Pacific Convergence Zones. *J. Geophys. Res. Atmos.* **121**(11), 590–607 (2016).

11. Arora, V. K. *et al.* Carbon–concentration and carbon–climate feedbacks in CMIP5 Earth system models. *J. Clim.* **26**, 5289-5314 (2013).

12. Sun, Y., Solomon, S., Dai, A. & Portmann, R. W. How often does it rain? *J. Clim.* **19**, 916-934 (2006).

13. Randall, D., Khairoutdinov, M., Arakawa, A. & Grabowski, W. Breaking the cloud parameterization deadlock. *Bull. Amer. Meteor. Soc.* **84**(11), 1547-1564 (2003).

14. Kooperman, G. J., Pritchard, M. S., Burt, M. A., Branson, M. D. & Randall, D. A. Robust effects of cloud superparameterization on simulated daily rainfall intensity statistics across multiple versions of the Community Earth System Model. *J. Adv. Model. Earth Syst.* **8**, 1-26 (2016).

15. Swann, A. L. S., Fung, I. Y. & Chiang, J. C. H. Mid-latitude afforestation shifts general circulation and tropical precipitation. *Proc. Natl. Acad. Sci. U.S.A.* **109**(3), 712-716 (2012).

16. Vecchi, G. A. & Harrison, M. J. Weakening of tropical Pacific atmospheric circulation due to anthropogenic forcing. *Nature* **441**, 73-76 (2006).

17. Kang, S. M., Held, I. M., Frierson, D. M. W. & Zhao, M. The response of the ITCZ to extratropical thermal forcing: Idealized slab-ocean experiments with a GCM. *J. Clim.* **21**, 3521-3532 (2008).

18. Held, I. M. & Soden, B. J. Robust responses of the hydrological cycle to global warming. *J. Clim.* **19**, 5686-5699 (2006).

19. Xie, S.-P., Deser, C., Vecchi, G. A., Ma, J., Teng, H. & Wittenberg, A. T. Global warming pattern formation: Sea surface temperature and rainfall. *J. Clim.* **23**, 966-986 (2010).

20. Byrne, M. P., & O'Gorman, P. A. The Response of Precipitation Minus Evapotranspiration to Climate Warming: Why the "Wet-Get-Wetter, Dry-Get-Drier" Scaling Does Not Hold over Land. *J. Climate*, **28**, 8078-8092 (2015).

21. Boos, W. R., & Korty, R. L. Regional energy budget control of the intertropical convergence zone and application to mid-Holocene rainfall. *Nature Geoscience*, **9**, 892-897 (2016).

22. van der Ent, R. J. & Savenije, H. H. G. Oceanic sources of continental precipitation and the correlation with sea surface temperature. *Water Resour. Res.* **49**, 3993-4004 (2013).

23. Cook, K. H. & Vizy, E. K. Effects of twenty-first-century climate change on the Amazon rainforest. *J. Clim.* **21**, 542-560 (2008).

24. Insel, N., Poulsen, C. J., & Ehlers, T. A. Influence of the Andes Mountains on South American moisture transport, convection, and precipitation, *Clim. Dyn.*, **35**, 1477-1492 (2010).

25. Fu R. *et al.* Increased dry-season length over southern Amazonia in recent decades and its implication for future climate projection. *Proc. Natl. Acad. Sci. U.S.A.* **110**(45), 18110-18115 (2013).

26. Arnold, N. P., Branson, M., Kuang, Z., Randall, D. & Tziperman, E. MJO intensification with warming in the superparameterized CESM. *J. Clim.* **28**, 2706-2724 (2015).

27. Turner, A.G. & Annamalai, H. Climate change and the South Asian summer monsoon. *Nat. Clim. Change* **2**, 587-595 (2012).

28. Pu, B. & Dickinson, R. E. Hydrological changes in the climate system from leaf responses to increasing CO_2. *Clim. Dyn.* **42**, 1905-1923 (2014).

29. Sellers, P. J. *et al.* Comparison of Radiative and Physiological Effects of Doubled Atmospheric CO_2 on Climate. *Science* **271**(5254), 1402-1406 (1996).

30. Cowan, I. R. Stomatal behaviour and environment. *Adv. Bot. Res.* **4**, 117-228 (1977).

31. Field, C. B., Jackson, R. B. & Mooney, H. A. Stomatal responses to increased CO_2: Implications from the plant to the global scale. *Plant Cell Environ.* **18**(10), 1214-1225 (1995).

32. Ball, J. T., Woodrow, I. E. & Berry, J. A. A model predicting stomatal conductance and its contribution to the control of photosynthesis under different environmental conditions. In: Biggins J (ed.) Progress in photosynthesis research. Springer Netherlands, pp 221-224 (1987).

33. Medlyn, B. E. *et al.* Stomatal conductance of forest species after long-term exposure to elevated CO_2 concentration: A synthesis. *New Phytologist* **149**(2), 247-264 (2001).

34. Medlyn, B. E. *et al.* Reconciling the optimal and empirical approaches to modeling stomatal conductance. *Global Change Biology* 17(6), 2134-2144 (2011).

35. De Kauwe, M. G. *et al.* Forest water use and water use efficiency at elevated CO_2: A model-data intercomparison at two contrasting temperate forest FACE sites. *Glob. Change Biol.* **19**, 1759-1779 (2013).

36. van der Sleen, P. *et al.* No growth stimulation of tropical trees by 150 years of CO_2 fertilization but water-use efficiency increased. *Nature Geoscience* **8**, 24-28 (2015).

37. Gedney, N. *et al.* Detection of a direct carbon dioxide effect in continental river runoff records. *Nature* **439**, 835-838 (2006).

38. Coe, M. T., Costa, M. H. & Soares-Filho, B. S. The influence of historical and potential future deforestation on the stream flow of the Amazon River-Land surface processes and atmospheric feedbacks. *Journal of Hydrology* **369**, 165-174 (2009).

39. Lindsay, K. *et al.* Pre-industrial-control and twentieth-century carbon cycle experiments with the Earth system model CESM1(BGC). *J. Clim.* **27**, 8981-9005 (2014).

40. Gill, A. E. Some simple solutions for heat-induced tropical circulation. *Quart. J. R. Met. Soc.* **106**, 447-462 (1980).

41. Cook, K. H., Hsieh, J.-S. & Hagos, S. M. The Africa–South America intercontinental teleconnection. *J. Clim.* **17**, 2851-2865 (2004).

42. Spracklen, D. V., Arnold, S. R., & Taylor, C. M. Observations of increased tropical rainfall preceded by air passage over forests. *Nature*, **489**, 282-285 (2012).

43. Inoue, K. & Back, L. Column-integrated moist static energy budget analysis on various time scales during TOGA COARE. *J. Atmos. Sci.*, **72**, 1856-1871 (2015).

44. Raymond, D. J., Sessions, S. L., Sobel, A. H., & Fuchs, Z. The mechanics of gross moist stability*, J. Adv. Model. Earth Syst.*, **1**(9), 1-20 (2009).

45. Vizy, E. K. & Cook, K. H. Relationship between Amazon and high Andes rainfall. *J. Geophys Res.* **112**(D07107), 1-14 (2007).

46. Malhi, Y. *et al.* Exploring the likelihood and mechanism of a climate-change-induced die back of the Amazon rainforest. *Proc. Natl. Acad. Sci. U.S.A.* **106**(49), 20610-20615 (2009).

Acknowledgments

G.J.K., Y.C., and J.T.R. acknowledge support from the Gordon and Betty Moore Foundation (GBMF3269). C.D.K., F.M.H., M.S.P., and J.T.R. acknowledge support from the US Department of Energy (DOE) Office of Science Biological and Environmental Research programs. The DOE support includes funding from the Regional and Global Climate Modeling program to the Reducing Uncertainties in Biogeochemical Interactions through Synthesis and Computation (RUBISCO) Scientific Focus Area, from the Terrestrial Ecosystem Sciences program to the Next Generation Ecosystem Experiments - Tropics, and from the Early Career program (DE-SC0012152). K.L. acknowledges support from the National Center for Atmospheric Research (NCAR), which is sponsored by the US National Science Foundation (NSF). A.L.S.S. acknowledges support from the NSF (AGS-1321745 and AGS-1553715). CESM development is led by NCAR and supported by the NSF and DOE. CESM simulations were run at the NSF NCAR Computational and Information Systems Laboratory on Yellowstone (P36271028). CESM output is available from G.J.K. (gkooperm@uci.edu) and archived at NCAR. CMIP5 simulation output is available on the Earth System Grid (http://esgf.llnl.gov).

Author contributions

All authors contributed to designing the experiment, interpreting the results, and editing the manuscript. G.J.K. performed the simulations, carried out the analysis, and drafted the manuscript. M.S.P. conducted the moist stability analysis.

Competing financial interests

The authors have no competing financial interests.

Methods

Experimental Design:

This study investigates precipitation changes in three sets of simulations. Evaluation of CMIP5 RCP8.5 simulations demonstrates that a zonally asymmetric tropical precipitation change pattern is ubiquitous in GCM simulations of the 21st century under a business as usual emissions scenario. Evaluation of idealized CMIP5 Earth system model simulations demonstrates that the physiological response of plants is the primary driver of this pattern over dense tropical forest regions. Evaluation of CESM simulations in which the CO_2 physiological forcing is applied over individual tropical continents demonstrates that locally driven changes in evapotranspiration and moisture convergence capture the majority of the pan-tropical precipitation change, with a small non-local contribution of reduced precipitation over the Amazon associated with the forcing over Central Africa. Each set of simulations, as well as the observations used for comparison, are described in detail below.

CMIP5 RCP8.5 Simulations:

This study evaluated output from thirty-eight models (references for each model are given in Table S2[47-82]) contributing historical and RCP8.5 simulations to CMIP5[7]. Both simulation sets use fully coupled model configurations with interactive atmosphere, land, ocean, and sea-ice components. Boundary conditions for the historical simulations included the observed time series of greenhouse gas concentrations and best-estimate time series of aerosol particle emissions. The RCP8.5 simulations were performed with increasing greenhouse gases and aerosol particle emissions from 2006 to 2100 (reaching approximately 1370 ppm CO_2-equivalent mole fraction

456 by 2100[83]). Averages from years 1986-2005 and 2081-2100 provide climatological conditions
457 for present and future periods, respectively (Table S4).
458
459 *CMIP5 ESM Simulations:*
460 This study also evaluates output from a CMIP5 experiment designed to assess carbon-climate
461 feedbacks[11]. Eight models (references for each model are given in Table S3) participated in this
462 experiment in which the concentration of CO_2 increased at a rate of 1% year^{-1} from 285 (pre-
463 industrial) to 1140 ppm ($4xCO_2$) for radiation and biogeochemistry (Full, 1pctCO2), radiation
464 only (Radiation, esmFdbk1), and biogeochemistry only (Physiology, esmFixClim1). In Radiation
465 and Physiology simulations, CO_2 was held at pre-industrial levels (285 ppm) for
466 biogeochemistry and radiation sub-models, respectively. Averages of the first and last twenty
467 years provide pre-industrial and future conditions, respectively (Table S4).
468
469 *CESM Simulations:*
470 We performed an additional set of new simulations using CESM1.0.6(BGC), applying the
471 biogeochemistry only CO_2 forcing to land surfaces globally (Physiology) and isolated over
472 tropical (23˚S – 23˚N) America, Africa, and Asia (black boxes in Fig. 1f). CESM is a fully
473 coupled Earth system model with active biogeochemistry[39], and the Community Atmosphere
474 Model[84] and Community Land Model[85] as atmospheric and land components, respectively. In
475 CESM, the representation of stomata conductance is based on the Ball-Berry model and is given
476 as the inverse of leaf stomatal resistance: $\frac{1}{r_s} = m\frac{A}{c_s}\frac{e_s}{e_i}P_{atm} + b$, where r_s is leaf stomatal
477 resistance, m is a plant functional type dependent parameter, A is leaf photosynthesis, c_s is the
478 CO_2 partial pressure at the leaf surface, e_s is the vapor pressure at the leaf surface, e_i is the

479 saturation vapor pressure inside the leaf, P_{atm} is the atmospheric pressure, and b is the minimum
480 conductance. For CESM simulations, an average of the twenty-years prior to increasing CO_2
481 provides pre-industrial conditions that are consistent for all cases. Averages of the last twenty
482 years of each case provide future conditions (Table S4).
483
484 *Superparameterized CCSM4 Simulation:*
485 Results from the Superparameterized Community Climate System Model version 4
486 (SPCCSM4) RCP8.5 simulation are also included in Fig. 1 and S1 (squares) and Table S2, but
487 are not used in the multi-model mean calculation (i.e., Table S1). The superparameterization
488 approach applies simplified cloud-resolving models to represent unresolved sub-grid moist
489 convection explicitly rather than using conventional convective parameterizations[13]. In the
490 SPCCSM4 simulation analyzed here, each column of the Community Atmosphere Model
491 contains an independent (i.e. periodic boundary conditions) two-dimensional cloud-resolving
492 model configured with 32 columns at 3 km resolution oriented in the east-west direction[82].
493
494 *Observations:*
495 We used observed present-day (2002 to 2011) precipitation and evapotranspiration data from
496 the Global Precipitation Climatology Project One-Degree Daily product (GPCP[86]) and Global
497 Land Evaporation Amsterdam Model product (GLEAM[87]), respectively.
498
499 *Regional Analysis (I_{TPA} and I_{TPA2}):*

500 The model output and observational data were interpolated to 0.25˚ resolution and a
501 consistent tropical forest and woodland mask (shown as the green areas in Fig. 1f) was used for
502 an area-weighted calculation of annual mean precipitation in each region.
503
504 *Gross Moist Stability Analysis:*
505 Gross moist stability was normalized (NGMS) using a simplified formulation following
506 equation 3 in *Inoue and Back*[43], with constituent variables estimated numerically using annual
507 mean fields pre-interpolated vertically onto a high-resolution (5 hPa) pressure grid, and with
508 centered finite differences to estimate vertical and horizontal (spherical) gradients of temperature
509 (T), water vapor (Q), and geopotential height (Z). Following *Benedict et al.*[88], a 7° × 7°
510 horizontal smoother was applied. NGMS was decomposed into horizontal and vertical
511 components following equation 4 in *Inoue and Back*[43]. This decomposition separates the changes
512 in horizontal winds (U and V) and moist static energy gradients (i.e., horizontal component)
513 from the changes in vertical winds (Omega) and moist static energy gradients (i.e., vertical
514 component). To determine the degree to which changes in circulation (i.e., dynamics) versus
515 changes in the vertical profiles and horizontal gradients of heat and water vapor (i.e.,
516 thermodynamics) control the total NGMS change, we further decompose the horizontal and
517 vertical components into dynamic and thermodynamic components. This decomposition is
518 achieved by calculating NGMS using the pre-industrial circulation from the control simulation
519 (i.e., U, V, and Omega) with Physiological thermodynamics (i.e., Q, T, and Z) for the
520 thermodynamic component and vice versa for the dynamic component. Results of the
521 decomposition are presented in Fig. 5c and 5d, and further discussion of this analysis is provided
522 in the Supplementary Information.

Data availability:

CMIP5 RCP8.5 and ESM output (precipitation variable: pr) is available on the Earth System Grid (http://esgf.llnl.gov). CESM output is available from G.J.K. (kooperman@uge.edu) and archived at NCAR. GPCP data is available from: http://precip.gsfc.nasa.gov, and GLEAM data is available from: http://www.gleam.eu.

References

47. Bi D. *et al.* The ACCESS Coupled Model: Description, control climate and evaluation. *Aust. Meteorol. Oceanogr. J.* **63**, 41-64 (2013).
48. Dix, M. *et al.* The ACCESS Coupled Model: Documentation of core CMIP5 simulations and initial results. *Aust. Meteorol. Oceanogr. J.* **63**, 83-99 (2013).
49. Gent, P.R. *et al.* The Community Climate System Model Version 4. *J. Clim.* **24**, 4973-4991 (2011).
50. Long, M. C., Lindsay, K., Peacock, S., Moore, J. K. & Doney, S. C. Twentieth-century oceanic carbon uptake and storage in CESM1(BGC). *J. Clim.* **26**, 6775-6800 (2012).
51. Hurrell, J. *et al.* The Community Earth System Model: A framework for collaborative research. *Bull. Am. Meteorol. Soc.* **94**, 1339-1360 (2013).
52. Fogli, P. G. *et al. INGV-CMCC Carbon (ICC): A Carbon Cycle Earth System Model. CMCC Res Papers*, Euro-Mediterranean Center on Climate Change, Bologna, Italy, 31pp (2009).
53. Vichi, M. *et al.* Global and regional ocean carbon uptake and climate change: Sensitivity to a substantial mitigation scenario. *Clim. Dyn.* **37**, 1929-1947 (2011).

54. Scoccimarro, E. *et al.* Effects of tropical cyclones on ocean heat transport in a high resolution Coupled General Circulation Model. *J. Clim.* **24**, 4368-4384 (2011).

55. Voldoire, A. *et al.* The CNRM-CM5.1 global climate model: Description and basic evaluation. *Clim. Dyn.* **40**, 2091-2121 (2013).

56. Rotstayn, L. D. *et al.* Aerosol- and greenhouse gas-induced changes in summer rainfall and circulation in the Australasian region: A study using single-forcing climate simulations. *Atmos. Chem. Phys.* **12**, 6377-6404 (2012).

57. Arora, V. K. *et al.* Carbon emission limits required to satisfy future representative concentration pathways of greenhouse gases. *Geophys. Res. Lett.* **38**(5), L05805 (2011).

58. von Salzen, K. *et al.* The Canadian Fourth Generation Atmospheric Global Climate Model (CanAM4). Part I: Representation of physical processes. *Atmos. Ocean* **51**, 104-125 (2013).

59. Hazeleger, W. *et al.* EC-Earth V2.2: Description and validation of a new seamless earth system prediction model. *Clim. Dyn.* **39**, 2611-2629 (2012).

60. Qiao, F. *et al.* Development and evaluation of an Earth System Model with surface gravity waves. *J. Geophys. Res. Oceans* **118**, 4514-4524 (2013).

61. Delworth, T. L. *et al.* GFDL's CM2 global coupled climate models. Part I: Formulation and simulation characteristics. *J. Clim.* **19**, 643-674 (2006).

62. Donner, L. J. *et al.* The dynamical core, physical parameterizations, and basic simulation characteristics of the atmospheric component AM3 of the GFDL Global Coupled Model CM3. *J. Clim.* **24**, 3484-3519 (2011).

63. Dunne, J. P. *et al.* GFDL's ESM2 Global coupled climate-carbon Earth System models. Part I: Physical formulation and baseline simulation characteristics. *J. Clim.* **25**, 6646-6665 (2012).

64. Dunne, J. P. *et al.* GFDL's ESM2 global coupled climate-carbon Earth System Models Part II: Carbon system formulation and baseline simulation characteristics. *J. Clim.* **26**, 2247-2267 (2013).

65. Schmidt, G. A. *et al.* Present day atmospheric simulations using GISS Model: Comparison to in-situ, satellite and reanalysis data. *J. Clim.* **19**, 153-192 (2006).

66. Collins, W. J. *et al.* Development and evaluation of an Earth-System model HadGEM2. *Geosci. Model Dev.* **4**, 1051-1075 (2011).

67. Martin, G. M. *et al.* The HadGEM2 family of Met Office Unified Model climate configurations. *Geophys. Model Dev.* **4**, 723-757 (2011).

68. Jones, C. D. *et al.* The HadGEM2-ES implementation of CMIP5 centennial simulations. *Geosci. Model Dev.* **4**(3), 543-570 (2011).

69. Dufresne, J.-L. *et al.* Climate change projections using the IPSL-CM5 Earth System Model: From CMIP3 to CMIP5. *Clim. Dyn.* **40**(9-10), 2123-2165 (2013).

70. Watanabe, M., Chikira, M., Imada, Y. & Kimoto, M. Convective control of ENSO simulated in MIROC. *J. Clim.* **24**, 543-562 (2011).

71. Watanabe, M. *et al.* Improved climate simulation by MIROC5: Mean states, variability, and climate sensitivity. *J. Clim.* **23**, 6312-6335 (2010).

72. Giorgetta, M. A. *et al.* Climate and carbon cycle changes from 1850 to 2100 in MPI-ESM simulations for the Coupled Model Intercomparison Project phase 5. *J. Adv. Model. Earth Syst.* **5**, 572-597 (2013).

73. Yukimoto, S. *et al. Meteorological Research Institute-Earth System Model v1 (MRI-ESM1) Model Description*. Technical Report of MRI, Ibaraki, Japan, 88pp (2011).

74. Yukimoto, S. *et al.* A new global climate model of the Meteorological Research Institute: MRI-CGCM3–Model description and basic performance. *J. Meteorol. Soc. Jpn.* **90A**, 23-64 (2012).

75. Adachi, Y. *et al.* Basic performance of a new earth system model of the Meteorological Research Institute (MRI-ESM1). *Papers Meteorol. Geophys.* **64**, 1-19 (2013).

76. Tjiputra, J. F. *et al.* Evaluation of the carbon cycle components in the Norwegian Earth System Model (NorESM). *Geophys. Model Dev.* **6**(2), 301-325 (2013).

77. Iversen, T. *et al.* The Norwegian Earth System Model, NorESM1–M. Part 2: Climate response and scenario projections. *Geosci. Model Dev.* **6**, 1-27 (2013).

78. Wu, T. A mass-flux cumulus parameterization scheme for large-scale models: Description and test with observations. *Clim. Dyn.* **38**, 725-744 (2012).

79. Xin, X., Wu, T., Li, J., Wang, Z., Li, W. & Wu, F. How well does BCC_CSM1.1 reproduce the 20th century climate change over China? *Atmos. Ocean Sci. Lett.* **6**, 21-26 (2012).

80. Xin, X., Zhang, L., Zhang, J., Wu, T. & Fang, Y. Climate change projections over East Asia with BCC_CSM1.1 climate model under RCP scenarios. *J. Meteorol. Soc. Jpn.* **91**, 413-429 (2013).

81. Volodin, E. M., Dianskii, N. A. & Gusev, A. V. Simulating present-day climate with the INMCM4.0 coupled model of the atmospheric and oceanic general circulations. *Izvestiya Atmos. Ocean Phys.* **46**, 414-431 (2010).

82. Stan, C. & Xu, L. Climate simulations and projections with a superparameterized climate model. *Environ. Modell. Software* **60**, 134-152 (2014).

83. Moss, R. H. *et al.* The next generation of scenarios for climate change research and assessment. *Nature* **463**, 747-756 (2010).

84. Neale, R. B. *et al. NCAR Technical note: Description of the NCAR Community Atmosphere Model (CAM 4.0)*. National Center for Atmospheric Research, Boulder, CO, U.S.A. (2010).

85. Lawrence, D. M. *et al.* Parameterization improvements and functional and structural advances in version 4 of the Community Land Model. *J. Adv. Model. Earth Syst.* **3**(M03001), 1-27 (2011).

86. Huffman, G. J. *et al.* Global precipitation at one-degree daily resolution from multi-satellite observations. *J. Hydrometeor.* **2**, 36-50 (2001). Accessed 2014 (http://precip.gsfc.nasa.gov).

87. Miralles, D. G. *et al.* Global land-surface evaporation estimated from satellite-based observations. *Hydrol. Earth Syst. Sci.* **15**, 453-469 (2011).

88. Benedict, J. J., Maloney, E. D., Sobel, A. H., & Frierson, D. M. Gross Moist Stability and MJO Simulation Skill in Three Full-Physics GCMs. *J. Atmos. Sci.*, **71**, 3327-3349 (2014).

Figures

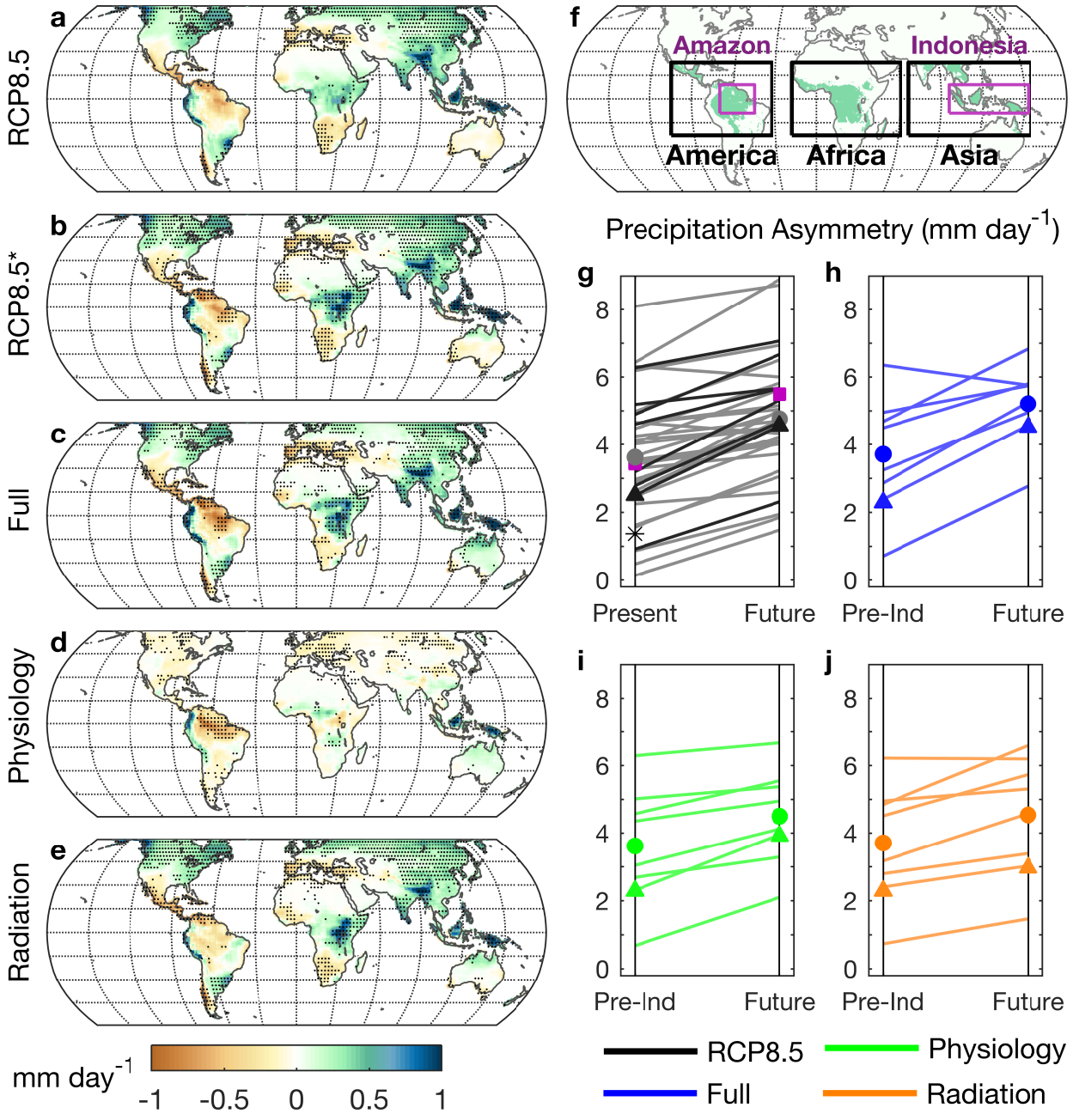

Fig. 1. Multi-model mean annual mean precipitation change and tropical precipitation asymmetry index. Changes from (**a**) RCP8.5, (**b**) RCP8.5* (sub-set of eight Earth system models used in other simulations), (**c**) Full, (**d**) Physiology, and (**e**) Radiation simulations (the

631 simulations are described in the text and Table S4), and (**f**) tropical forests regions used to
632 calculate the (**g-j**) tropical precipitation asymmetry index (I_{TPA}). RCP8.5 results are differences
633 between 2081-2100 and 1986-2005, while other simulations are differences between $4xCO_2$ and
634 pre-industrial periods. Stippling in **a-e** indicate where 87.5% of models have the same sign of
635 change (this measure of uncertainty does not account for multiple contributions of different
636 model versions[10]). Symbols in **g-j** are mean results for all CMIP5 models (circles), CESM
637 (triangles), Superparameterized CCSM4 (purple squares), and observations (star).
638

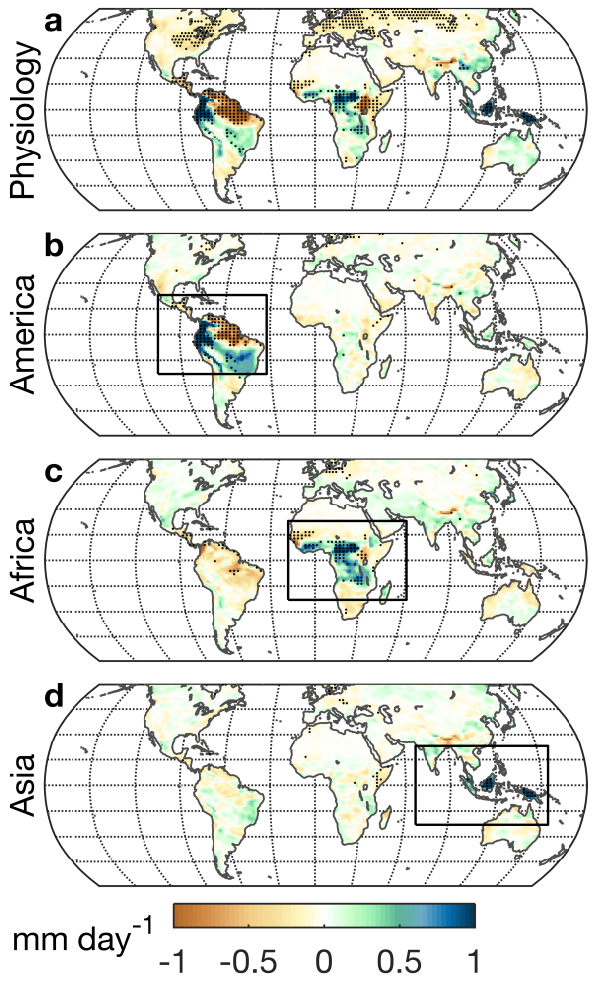

639

640 **Fig. 2. Annual mean precipitation change from the Community Earth System Model.**

641 Changes from CESM (4×CO_2 minus pre-industrial) for (a) Physiology, (**b**) America, (**c**) Africa,

642 and (**d**) Asia simulations. All simulations include only the physiological forcing, which is

643 applied regionally in **b-d**. Stippling in **a** indicates 90% confidence based on interannual

644 variability, and stippling in **b-d** indicates where the sign and magnitude of the precipitation

645 change in the regional simulation is at least 50% of statistically significant change in the global

646 Physiology simulation.

647

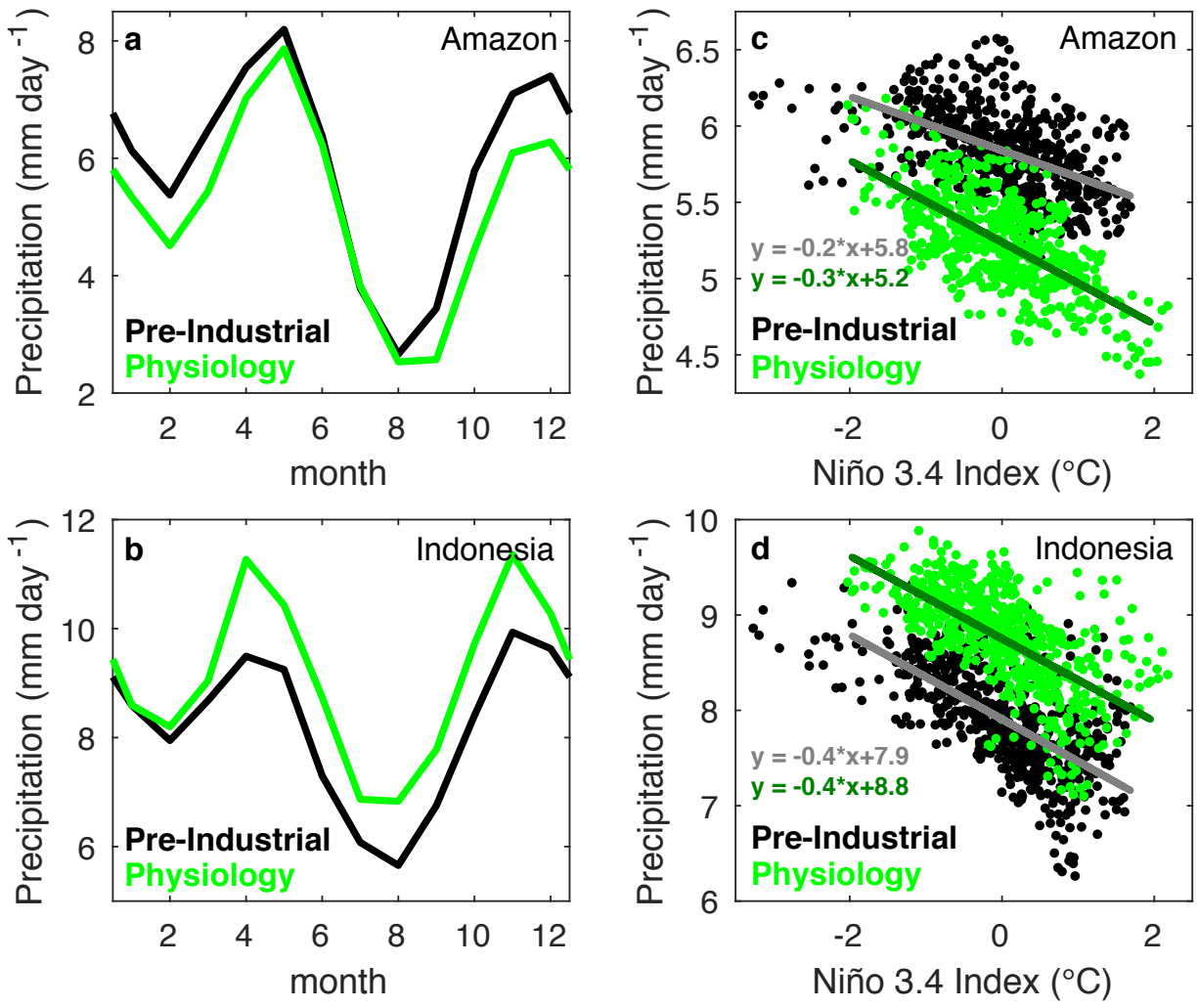

Fig. 3. Precipitation (a/b) seasonal cycle and (c/d) Niño 3.4 index relationship over the (a/c) Amazon and (b/d) Indonesian forest regions. Results are from global Physiology (green) and Pre-industrial control (black) simulations. Niño 3.4 index analysis is based on extended simulations for an additional fifty-years with fixed pre-industrial and 4xCO_2 concentrations. The Niño 3.4 index is formed from five-month running-mean monthly surface temperature anomalies within the region between 170˚W-120˚W and 5˚S-5˚N, which is regressed against twelve-month running-mean monthly precipitation in the Amazon and Indonesian regions as defined in the text. Regressions are linearly fit for the Physiology (dark green) and Pre-industrial (gray) simulations.

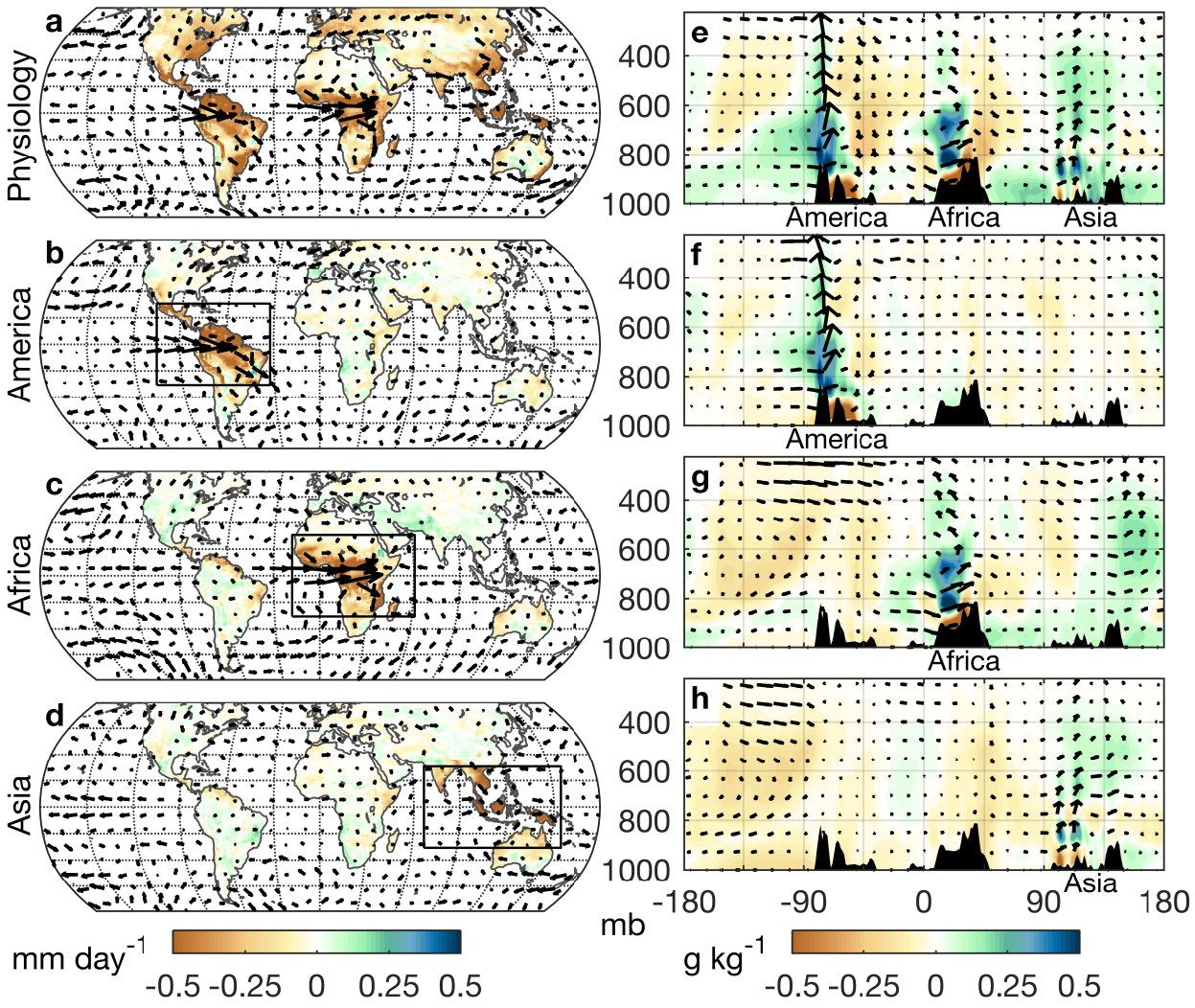

Fig. 4. Annual mean evapotranspiration (a-d) and tropical (5˚S-5˚N) meridional mean specific humidity (e-h) change. Changes from CESM (4×CO_2 minus pre-industrial) for (**a/e**) Physiology, (**b/f**) America, (**c/g**) Africa, and (**d/h**) Asia simulations. Arrows in **a-d** show the change in 850mb horizontal wind and arrows in **e-h** show the change in meridional mean zonal and vertical (omega) circulation with pressure as the vertical coordinate.

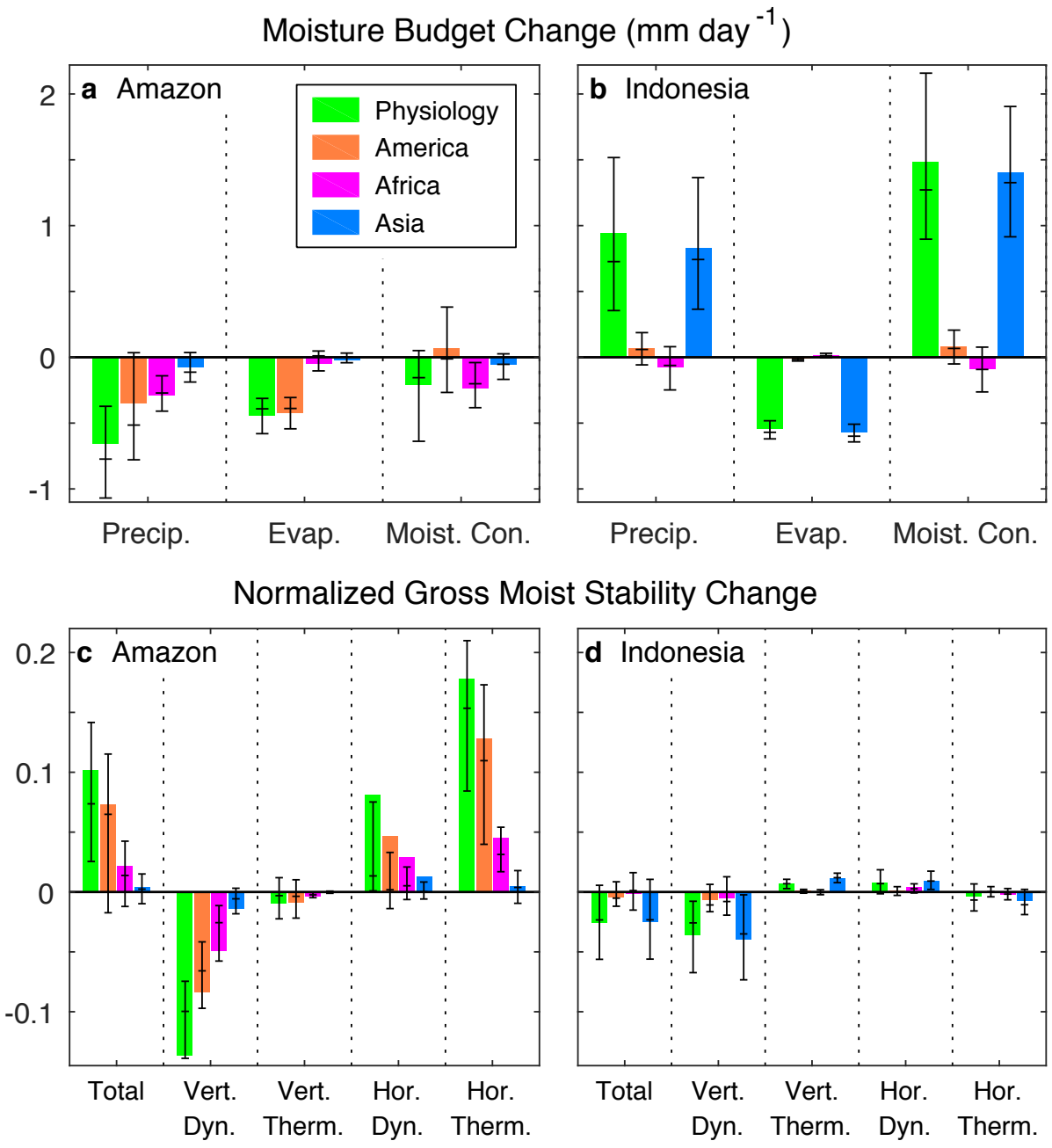

Fig. 5. Annual mean moisture budget (precipitation, evapotranspiration, and moisture convergence) and normalized gross moist stability changes. Changes ($4\times CO_2$ minus pre-industrial) are averaged over the (**a/c**) Amazon and (**b/d**) Indonesian forest regions (purple boxes in Fig. 1f) from CESM for Physiology, America, Africa, and Asia simulations. The normalized gross moist stability changes in panels **c/d** are further decomposed into vertical-dynamic,

671 vertical-thermodynamic, horizontal-dynamic, and horizontal-thermodynamic components as
672 described in the methods section. Bracketed lines indicate the inter-quartile range (25^{th}, 50^{th}, and
673 75^{th} percentile values) based on the spatial variability from grid-points used in the regional
674 average.
675